Highly flexible superconducting films with metal-decorated composite 2D materials

Pauline Ronseaux[1], Riadh Othmen[1], Dipankar Kalita[1], Zheng Han[1], Laëtitia Marty[1], Nedjma Bendiab[1], Julien Renard[1] and Vincent Bouchiat[1]

[1]Univ. Grenoble Alpes, CNRS, Grenoble INP, Institut Néel, 38000 Grenoble, France

E-mail: `vincent.bouchiat@neel.cnrs.fr`

Abstract. Graphene forms an ideal platform to realize macroscopic hybrid materials by direct physisorption of electronically-active adsorbates on top of the high-mobility bidimensional (2D) gas of charge carriers. Here, we demonstrate a novel composite multilayer based on a thin polymer film covered with a monolayer of CVD graphene on top of which a metallic thin-film of tin is evaporated. The metal film shows dewetting and forms a self-organized network of metal dots electronically coupled to the graphene underlayer. The resulting macroscopic multilayered structure is a highly flexible, stable and processable composite 2D material that exhibits tunable superconductivity at low temperature. The superconducting properties of the macroscopic composite (exceeding at least several square centimeters) are comparable to the ones of a mesoscopic array of Josephson junctions prepared with similar materials and provide an upscaling of the concept, that is useful for flexible electronics.

Keywords: CVD, Graphene, Flexible electronics, Hybrid devices, Metal deposition, Composite 2D materials, 2D superconductivity, Proximity effect

Submitted to: *2D Mater.*

1. Introduction

In bulk materials, combining organic and inorganic compounds has appeared as a productive method to obtain hybrid composites. The rationale behind such combination is that organic and inorganic materials usually have complementary properties that could together lead to multifunctional materials with novel features. The resulting properties go well beyond a simple combination of the individual properties of the original phases as a mutual synergy can occur and produces new features that are lacking in the parent-constituent materials. Indeed they depend on the size and morphology of the phases and the nature of their interaction [1].

Many mechanical deformations, such as crumpling or twisting, are usually considered as threats to mechanical integrity of traditional materials and structures. Three dimensional (3D) composites have thus been developed and have become indispensable in engineering, where they offer the advantage of low weight but high strength, and durability [2]. Examples of such realizations are numerous. For instance, the polymer industry allowed to obtain stable and robust composite materials by incorporating inorganic building blocks into a polymer matrix [3]. Extending this idea of combining different types of materials with sometimes antagonist properties (inorganic/organic, soft/hard, conducting/insulating) down to two dimensional (2D) materials is interesting as the low dimensionality reinforces the resilience to mechanical deformations and bring novel features that are usually absent in three dimensional composites, such as electronic quantum confinement. In that respect, graphene is ideal to form thin composite films since its absence of bulk allows maximal interaction with the other constituents and a direct virtually barrier-free electrical contact. Graphene-based composites are particularly interesting since they offer a new way to further exploit graphene exceptional properties, such as mechanical resilience, surface conductivity and electric field effect. Theoretical works predicted the emergence of superconducting correlations in graphene decorated with arrays of superconducting islands [4]. The resulting superconducting proximity effect and its gate tunability has been demonstrated experimentally and has shown to be a source of gate tunable 2D superconductor [5] and a model system to study the superconducting-to-insulator transition [6]. In these previous works, samples of limited area ($<$mm^2) were studied. We propose here to extend this concept of tunable superconductivity up to the scale of a macroscopic material ($>$cm^2) by exploring how flexible large scale graphene-based composite films can be produced.

We propose a macroscopic flexible thin composite film formed from 3 original compounds stacked together: organic (polymer plastic film) and inorganic (metal) materials are linked together through a CVD-made, monolayer (ML) graphene (semi-metal) sandwiched in between them. The organic polymer is composed of a few-μm-thick parylene layer, also named poly-para-xylylene. This chlorinated-type C parylene is a soft, stress-resilient material with a bending rigidity [7] much lower than commonly used substrates such as silicon [8]. Furthermore it can provide a mechanically stable substrate with typical thicknesses as thin as few micrometers. The inorganic compound

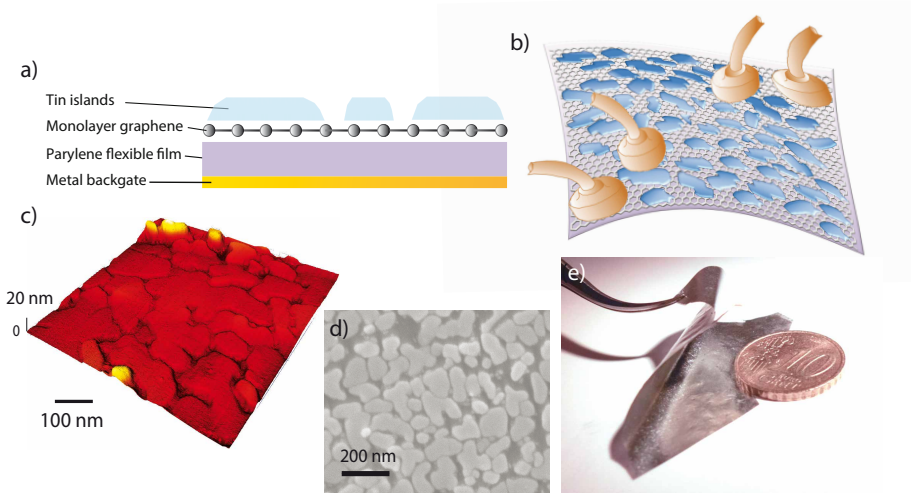

Figure 1. Schematics of the composite film. a-b) Schematics of the device showing the parylene-supported graphene decorated with the metallic tin dots. Optional back-metallisation of the parylene film enables the implementation of an electrostatic gate to study the field effect of the transport properties. c) Atomic Force and d) Scanning Electron micrographs of a typical sample. e) Macrophotography of a several centimeter square superconducting flexible composite film.

is based on an array of non-percolating adsorbates made of type-I superconducting, few-nm-thick, nanoparticles of tin (Sn). The graphene monolayer supported by the organic parylene substrate provides a two-dimensional gas of charge carriers to connect together the tin nanoparticles. The flexibility of thin parylene C substrate, reinforced by the very high mechanical strength of the graphene interface [9] and preserved by the discontinuity of the layer of tin, ensures the mechanical cohesion of the composite film. Thus, it is possible to repeatedly deform the composite film without fracturing unlike rigid materials (see Fig.1).

In the low temperature regime, the composite film exhibits long range superconducting correlations over the whole macroscopic interface of the tin-decorated graphene. The hybrid mix between the superconducting properties of the tin-decorated graphene and the properties of the parylene substrate, including high-flexibility and thermal insulation is typical of the plastic-like superconductors class [10, 2, 11]. We will show here that this new hybrid material brings an additional key characteristic: the possibility of a control with an electric field.The processability of this macroscopic composite film paves the way for applications such as flexible hybrid electronics [12, 13] and for thermal and vibrational insulating of cryogenic wiring. The fabrication methods and the measurement setup will be described first. Secondly, the electronic contribution of each compound will be determined using Raman spectroscopy. Thirdly, electron transport properties will be described in details. Finally, we will discuss the peculiar properties that appear in a perpendicular magnetic field and their potential applications.

2. Techniques and Methods

2.1. Material fabrication

The process to combine the three compounds consists in growing graphene by chemical vapour deposition (CVD) on a copper substrate [14] and depositing a several μm-thick layer of parylene on the graphene by vaporisation [15]. The copper substrate is then back-etched in a following step in order to provide a stable graphene-on-parylene film. Finally, tin film is thermally evaporated under vacuum. Spontaneous dewetting of this metallic film leads to a random array of graphene supported tin nanoparticles with reproducible sized gaps of approximately 20nm width. This natural phenomenon resulting from the high surface diffusion of metal on graphene leads to a hybrid system with remarkable homogeneity avoiding any use of lithographic step. Details of the fabrication are provided in the supplementary informations. The composite is sketched in Fig.1. Two samples have been studied: *Sample*1 (15nm Sn/ML graphene/4μm parylene) and *Sample*2 (20nm Sn/ML graphene/10μm parylene). Most of the results presented in the main text were obtained on *Sample*1. The initial samples size was tens of cm^2. They were cut into pieces of about 1 cm^2 to fit the size of the sample holders.

2.2. Measurement setup

In this work, we probed the electronic properties of the samples by varying different external parameters. The cryogenic environment was provided by a dilution refrigerator, which allowed to vary the temperature from 100mK up to 300K. The direct bias current (DC) was supplied by a programmable DC source Yokogawa 7651. A superconducting coil was used to create a transverse magnetic field. The electric field, source of charge carrier modulation, was applied with a back gate on the back-metalized parylene substrate. The electrical contacts on the devices were done with silver paste. Four probes measurements of the differential resistance have been performed using standard low frequency lock-in techniques.

3. Results

3.1. Raman analysis

Raman spectroscopy was performed at 532 nm on *Sample*1 before and after tin evaporation on top of graphene. The spectra are shown in Fig.2 a). Before tin deposition, the Raman spectrum (red line in Fig.2 a), c), and d)) exhibits several peaks corresponding to Raman modes of both graphene and parylene. The peaks at 321.9$\pm$1 cm^{-1}, 691.6$\pm$1 cm^{-1}, 876.1$\pm$1.7 cm^{-1}, 913.3$\pm$1 cm^{-1}, 1005.5$\pm$1 cm^{-1}, 1208.9$\pm$1 cm^{-1}, 1336.8$\pm$1 cm^{-1} and 1441.0$\pm$1 cm^{-1} are attributed to parylene C. The last mentioned three peaks have already been observed in previous studies reported in the literature [17, 18]. The peaks at 1599.6$\pm$1 cm^{-1} and 2695.9$\pm$1 cm^{-1} correspond to the G and 2D-modes of the graphene, respectively. The overlap of the G-mode with a supplementary

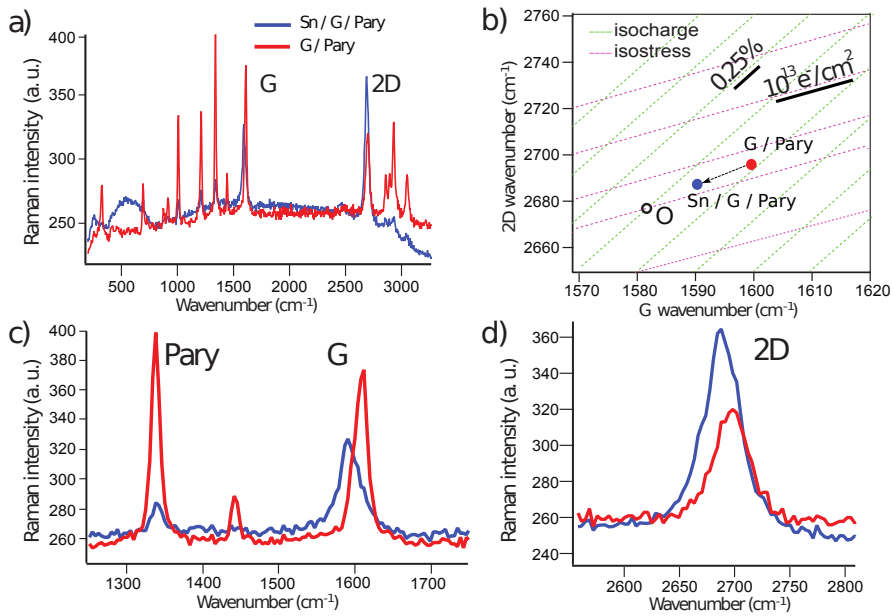

Figure 2. Raman spectroscopy of Sample 1. a,c and d) Raman spectra acquired before (red curves) and after tin deposition (blue curves) on the graphene (G)/parylene(Pary) composite film. b) Correlation between the G and 2D Raman modes (ω_G ; ω_{2D}) before (red point) and after (blue point) tin deposition. The isostress lines (magenta) with a slope of 0.7±0.05 represent (ω_G ; ω_{2D}) for strain-free graphene doped with varying density of holes. The isocharge lines with a slope of 2.2±0.2 represent (ω_G ; ω_{2D}) for graphene under variable uniaxial stress [16].

parylene C mode near 1610 cm^{-1} has been highlighted in the litterature [18]. The G-peak position has been determined by fitting the correspondinG-peak with a double lorentzian profile. One of the two lorentzian has been fixed at 1609.1 cm^{-1}, which corresponds to the position of the parylene C peak extracted from a Raman spectrum measured on C parylene without graphene (not shown). Note that this procedure can induce some uncertainty on the G-peak position.

After tin deposition (blue line in Fig.2a),c),and d)), the positions of the parylene C modes are essentially unaffected although their intensity is attenuated due to the screening effect induced by the metallic tin nanoparticules. The parylene C mode at 1441.0±1 cm^{-1} is the only one not observable after tin deposition (see Fig.2 c)) because its intensity does not overcome the noise.

On the other hand the G and 2D-modes of graphene are shifted. Fig.2 c) and *d*) are zoomed views of the G and 2D shifts. The wavenumbers of these two modes (ω_G ; ω_{2D}) are: (1599.6±1 cm^{-1} ; 2695.9±1 cm^{-1}) before and (1590.3±1 cm^{-1} ; 2687.3±1 cm^{-1}) after tin deposition. The G and 2D Raman modes (ω_G ; ω_{2D}) are both sensitive to induced strain [19, 20, 21, 22] and charge doping [23, 24]. The comparison of these two modes before and after tin deposition allows to determine to what extent each physical mechanism is responsible for their shifts [16]. The wavenumbers of the graphene Raman modes are reported on the ω_G-ω_{2D} plane featured in Fig.2b). The analysis presented

here follows the ones developed by Lee *et al.* [16] and Das *et al.* [24].

The O point in Fig.2b) is the expected postition of (G;2D) peaks for a neutral stress-free graphene [16]. Starting from this origin O, strain and doping induce shifts represented by unit vectors that are non-orthogonal in the (ω_G ; ω_{2D}) basis. The isostress lines (magenta) represent the effect of p-doping. The isocharge lines (green) represent a prediction of the wavenumbers (ω_G ; ω_{2D}) evolution under uniaxial stress. The uniaxial strain sensitivity of the G-mode is -23.5cm^{-1}/% [16, 25]. The red and blue points correspond to the experimental positions of the two modes before and after tin deposition, respectively.

The slope from the O point to the red point shows that the positions of the G and 2D-peaks before tin deposition are mostly imposed by a doping effect. It could mean that the parylene C induces weak stress but high p-doping. Recent studies [26] highlighted also a significant p-doping for graphene encapsulated with parylene C. Based on that assumption, the induced p-doping can be deduced comparing the distance from the O point to the red point along the isostress lines with the corresponding isostress scale bar. From Fig.2b), we get an induced p-doping around $1.3.10^{13}$ cm^{-2}. According to Das *et al.* [24], the 2D-peak position before tin deposition corresponds to a p-doping about $1.5.10^{13}$ cm^{-2}, which is coherent with our assumptions. These similarities with litterature strengthened the hypothesis of stress-free high p-doping induced by the parylene C before tin deposition.

An analysis based on the plot shown in Fig.2b) in order to determine the amount of doping and stress after tin deposition (blue point) would not be entirely satisfactory since the isostress lines (magenta), only valid for a p-doping case, and the isocharge lines (green) are experimentally determined [24, 16, 27] and may present some variations according to the experimental conditions. Nevertheless, the decrease of the position of the 2D-peak after tin deposition is a signature of an increase of electron concentration in the film [24]. We can reconcile this with the expected electron transfer from tin adsorbates to graphene that was observed in tin-decorated devices based on graphene exfoliated on oxidized silicon substrates by studying the electric field effect on the sample conductivity [5].

Taking into account this doping, the G-peak position after tin deposition corresponds to a holes density of about $0.5.10^{13}$ cm^{-2} or to an electrons density of about $0.8.10^{13}$ cm^{-2}[24]. But as this shift is non-monotonic in function of charges, it does not allow us to determine if the composite film is hole or electron doped. The variation of the conductance G at 4K in function of the residual doping in electrons Δn for $Sample1$ (see inset on Fig.3b)) allows to lift the ambiguity since it demonstrates that the composite film is electron doped after tin deposition.

From a line fit of the $G(\Delta n)$ curve, the residual doping at zero gate voltage is estimated to be $5.85.10^{12}$ cm^{-2}. This value is in accordance with the value previously estimated from the position of the G-peak after tin deposition. The discrepency is likely due to the difference in experimental conditions between the two types of measurements. All this analysis shows that the 2D and G-peak shifts induced by the tin deposition are

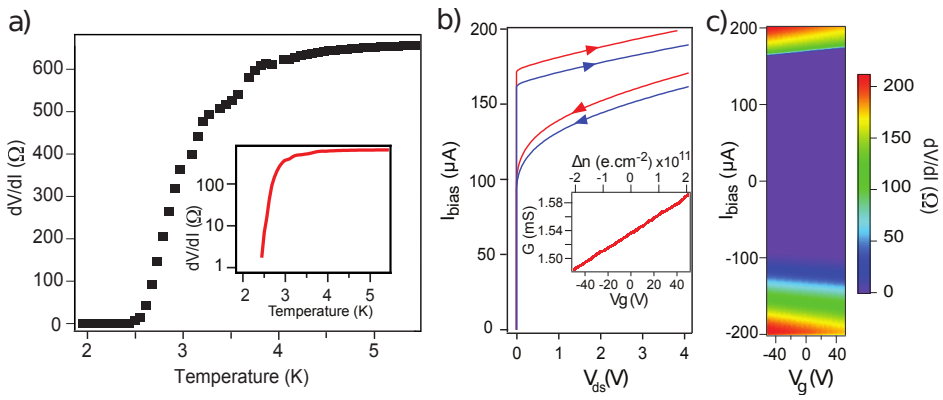

Figure 3. Temperature dependence and field effect for Sample 1 a) Temperature dependence of the differential resistance showing the gradual superconducting transition. The log scale used for the inset highlights the decrease of the differential resistance. b) Relationship between the drain-source voltage (V_{ds}) and the bias current (I_b) at 200 mK and at two gate voltage values, V_g=+50V (red curve) and V_g=-50V (blue curve). The inset displays the variation of the conductance (G) with the gate voltage (V_g) at 4 K. c) Evolution of the differential resistance with the gate voltage (V_g) and the bias current (I_b) at 200 mK.

mostly due to n-doping effect. Thus, the Raman spectra after tin deposition displayed on Fig.2a), c) and d) (blue lines) (ω_G=1590.3±1 cm^{-1} ; ω_{2D}=2687.3±1 cm^{-1}) corresponds to a Fermi level above the Dirac point.

3.2. Temperature dependence

Upon cooling, *Sample*1 exhibits a two-steps transition to the superconducting state. The first resistance drop at 3.7K in the differential resistance $\frac{dV}{dI}$ shown in Fig.3a) corresponds to the superconducting transition of the individual tin islands. This temperature is also the bulk critical temperature T_c of tin [28, 29], meaning that the intrinsic superconducting properties of the tin islands are almost unaffected. The composite film reaches then a resistance-less state after another wide drop at 2.4K which corresponds to the transition of the whole tin decorated graphene sample to a superconducting state, which is driven by the superconducting proximity effect.

3.3. Field effect

The Josephson effect in graphene has been previously studied by measuring superconductor/Normal/Superconductor (SNS) junctions consisting of a graphene layer contacted by two superconducting electrodes [30, 31]. In such systems the superconducting proximity effect in graphene is locally generated from the contacting electrodes and gives rise to a supercurrent carried either by electrons in the conduction band or by holes in the valence band of graphene, depending on the doping. It has

been shown that the proximity induced superconducting correlations can be controlled by means of a gate electrode. This gate tunable superconducting proximity effect in graphene was also demonstrated for a mesoscopic 2D network of superconducting tin clusters [6, 5]. In these previous studies on graphene-based Josephson junctions arrays, the gate voltage was applied through a stiff substrate made of a silicon oxide dielectric.

As the samples of the composite film studied in this work have a surface of typically a fraction of square centimeter, a billion of Josephson junctions can be probed thanks to the high density of the dewetted tin islands (about 100 per micron square, see section 1.3 in Supplementary informations). The high breakdown voltage of the order of 1V/nm of the parylene C [17], its small thickness of a few micrometers and its 20nm gold back-metallization make it possible to apply an electric field to tune the density of the charge carriers. At low temperature, these charge carriers convey the superconducting current in graphene between the superconducting tin adsorbates.

We next focus on the field effect dependence in $Sample1$. We measure a variation of the conductance G by about 7% for a gate voltage (V_g) span of 100V at 4K, above the superconducting transition (see the inset on Fig.3b)). As the parylene C substrate thickness for $Sample1$ is $4\pm0.5\mu$m, its estimated geometric capacitance C_s is about 6.6 10^{-10} F.cm^{-2}(see Supplementary informations). Due to residual doping, the material is n-doped in the whole gate voltage range and the neutrality point is not accessible in the inset on Fig.3b). The extension by proximity effect of the superconducting correlations from the vicinity of the tin islands to the whole decorated graphene interface depends on the electrostatic doping [6]. The CVD graphene charge carrier mobility of about 1640 cm^2.V^{-1}.s^{-1} (deduced from the inset on Fig.3b), see Supplementary informations for more details) makes the graphene interface a suitable mediator to couple tin islands.

The evolution of the drain-source voltage (V_{ds}) was probed by varying the bias current (I_b) for different gate voltages (V_g) at a temperature T=200mK, well below the critical temperature of tin (3.7K) [28, 29] (see Fig.3b)). For a fixed gate voltage (V_g), the $I_b(V_{ds})$ curve in Fig.3b) features a superconducting vertical branch at zero drain-source voltage (V_{ds}). In that region the charge carriers can flow through the whole sample without dissipation, giving rise to a supercurrent. When the bias current (I_b) is increased until the switching current (I_s), a sudden change to a resistive branch can be seen: this is the superconducting to normal state transition. This behaviour is characteristic of the regime in which the energy scale for the superconducting coupling between islands that permits transport of Cooper pairs, named Josephson coupling energy E_J, is much larger than the energy scale that tends to localize charge carriers, the charging energy E_C [32]. In the superconducting state, the switching current I_s is electrically tunable as illustrated in Fig.3b) and c). It is modulated by 100nA/V. This modulation may be enhanced by reducing the thickness of the parylene substrate.

3.4. Hysteretic behaviour

Fig.3b) highlights the hysteretic behaviour of the superconducting transition. When the bias current (I_b) is decreased from the normal resistive state to reach the superconducting state, the return to zero for the drain-source voltage (V_{ds}) only occurs at a retrapping current (I_r), which is significantly smaller than the switching current (I_s). Like the switching, the retrapping appears as a discontinuity of the $I_b(V_{ds})$ curve in Fig.3b). In other words, once the decorated graphene has switched to the resistive branch, it does not recover the superconducting state until the bias current is decreased to a significantly smaller retrapping current (I_r). For instance, at a gate voltage V_g=+50V (red curve in Fig.3b)), the switching current I_s is 172μA whereas the retrapping current I_r is 95μA. Hence, the curve in Fig.3b) is hysteretic.

The Joule power dissipation may largely contribute to that hysteretic phenomenon, as already suggested by previous studies of the self-heating of various types of superconducting weak links [33, 34]. Experimental works have demonstrated that the hysteresis in a SNS junction results from the increase of the normal-metal electron temperature (T_e) once the junction switches to the resistive state by measuring an electron temperature up to more than ten times the thermal bath temperature [35]. Hysteresis is increased when the switching current (I_s) is large. As the composite film is made of an array of graphene-based junctions and exhibits a large switching current (I_s), Joule dissipation inside graphene could be one of the mechanisms responsible for the observed hysteresis. Indeed, the Joule power $Rn.I_s^2$, where R_n≈650Ω and I_s≈ 170 μA are respectively the normal state resistance and the switching current at 4K and zero gate voltage, is estimated of the order of 20μW. This value is around 4.10^5 times more than the one estimated from [35]. In addition, the low thermal conductivity of the parylene C substrate (0.084 W·m^{-1}·K^{-1} at 25°C) [36] does not allow an efficient evacuation of the resulted heat and maintains the hysteretic phenomena. The hysteresis proves that the composite film has an ultra-low thermal conductivity. It may be an advantage in a cryogenic context.

3.5. Magnetic field dependence

*Sample*1 thickness allows a high sensitivity to a magnetic field perpendicular to its plane and makes thus possible to magnetically tune the superconducting transition. As one can see in Fig.4c), when no bias current is applied ($I_b = 0nA$), the magnetic field for which the SNS junction array undergoes a transition between its superconducting state and its normal state is about 100mT. This value is the critical magnetic field H_c for *Sample*1. Whenever the perpendicular magnetic field is above (H_c), the SNS junctions array differential resistance ($\frac{dV}{dI}$) never falls to zero for any bias current value. The evolution of the differential resistance ($\frac{dV}{dI}$) with the bias current (I_b) for a perpendicular magnetic field just above H_c is represented by the black line in Fig.4b). While the critical temperature of tin islands in our device is unchanged compared to the bulk value as discussed in section 3.2, the critical magnetic field (H_c) is much larger than the bulk

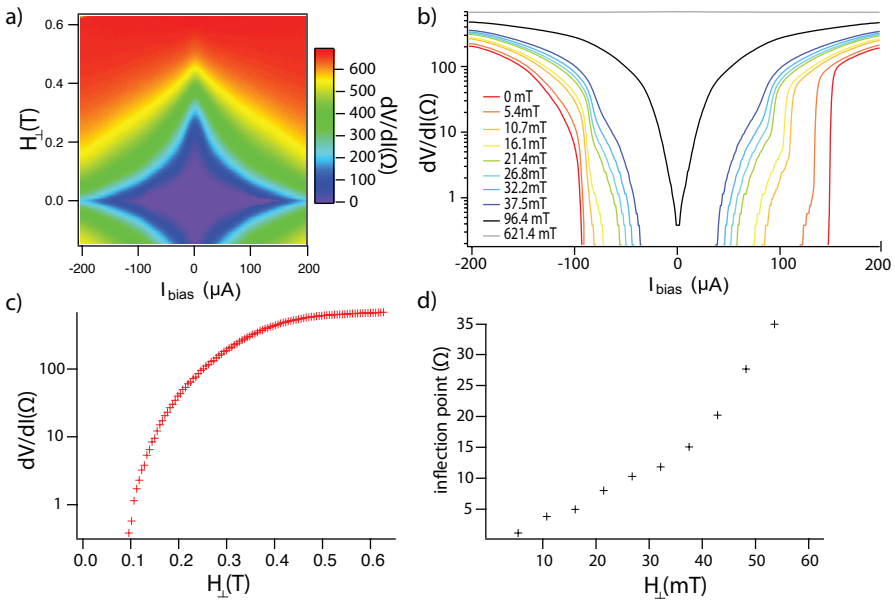

Figure 4. Perpendicular magnetic field dependence for Sample 1. a) and b) SNS junctions array differential resistance $\frac{dV}{dI}(I_b)$ as a function of transverse magnetic field ($H_\perp$) and bias current (I_b). c) SNS junctions array differential resistance $\frac{dV}{dI}(I_b)$ as a function of transverse magnetic field ($H_\perp$) in the absence of bias current ($I_b = 0$ nA). d) SNS junctions array differential resistance $\frac{dV}{dI}(Ib)$ at the switching current I_s, *i.e.* at the onset of a sharp transition towards the normal state.

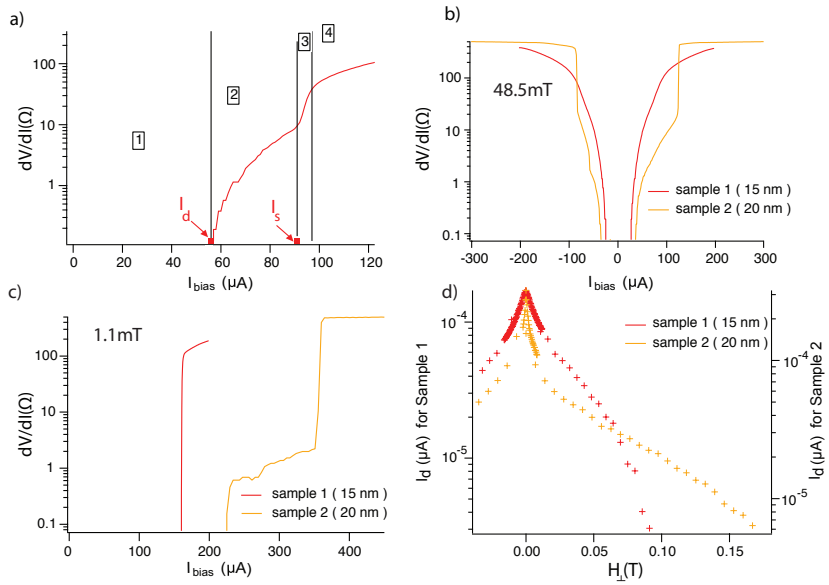

Figure 5. Vortices motion effect and dependence with metal thickness. a) Vortices motion dependent superconducting transition in $Sample1$. b) Hysteretic behaviour of the superconducting transition for $Sample1$ (red curve) and $Sample2$ (orange curve) ($H_\perp = 48.5mT$). c) Superconducting transition for $Sample1$ (red curve) and $Sample2$ (orange curve) at weak magnetic field ($H_\perp = 1.1mT$). d) Evolution of depinning current (I_d) with the perpendicular magnetic field.

critical magnetic field of Sn, which has been measured to be of the order of 30mT [37]. Previous studies of tin superconductivity at the nanoscale were carried out on Sn nanostructures. These studies found no departure from the bulk critical temperature T_c = 3.7 K in nanostructures, but in all cases found an overall increase of the critical field (H_c) with the decrease of particle size [38].

When no perpendicular magnetic field is applied, the density of supercurrent (J_s) can be estimated by normalizing the switching current (I_s) with the diameter of our probes of 1mm. Since, when there is no applied perpendicular magnetic field, the switching current (I_s) is 147 μA, the density of supercurrent $J_s = 1.47.10^2 nA \cdot \mu\text{m}^{-1}$. This value corresponds to the density of supercurrent measured for single Josephson junctions [39] and shows that the the critical behaviour of the macroscopic composite film corresponds to the one of a single Josephson junction (see section 2 in Supplementary informations).

4. Discussion

4.1. Sensitivity to magnetic field: effect of vortices motion

As shown in Fig.4b), for non zero magnetic field below the critical field H_c, the composite film presents a broad transition as a function of the bias current. The broadening of this transition has been attributed in previous studies to the dynamics of the vortices inducing a progressive dissipation until reaching the normal state [40, 41]. Focusing on the transition from the superconducting to the normal state in the presence of magnetic field in the positive bias current quadrant, we can notice four regions, as delimited in Fig.5a). In the low bias current regime, *i.e. region 1* in Fig.5a), the vortices are pinned and the composite film has zero differential resistance. Numerical simulations have studied the impact of defects in this context [42, 43]. The enhancement of the superconducting current near the tip of the defects gives rise to the formation of vortices that remain pinned to each end of the defects. In our case, the defects could be regions with weaker superconducting state. When the bias current (I_b) reaches the depinning current (I_d), the Lorentz force perpendicular to the bias current (I_b) is high enough to unpin and thus governs the vortices motion [43]. Their creeping produces a voltage across the sample which begins to present a non-zero differential resitance that increases with the bias current (I_b). We attribute the hill-shaped beginning of the transition in *region 2* to this creeping regime. The macroscopic switching current (I_s) is identified as the inflection point ending *regions 2*, *i.e.* when a sharp transition towards the normal state begins. In *region 2*, the hill-shaped curve does not end with a plateau as it has been observed experimentally in other types of Josephson junctions arrays [40]. It means that the motion of the vortices does not reach a constant speed before entering *region 3*. In *region 4*, the curve converges progressively towards the normal state differential resistance value. There is no peak in the resistance close to the switching current (I_s) as often observed in Josephson junctions. This is likely caused by the importance of

thermal effects and such behavior has already been observed in tin-decorated graphene hybrids. [5].

When the applied magnetic field is increased, the differential resistance ($\frac{dV}{dI}$) at the macroscopic switching current (I_s) featured in Fig.4d) is larger and the transition displayed in Fig.4b) broadens. As each vortex carries a quantum of flux [43], the increase of the applied magnetic field induces the proliferation of the number of vortices. Therefore, the magnetic field dependency of the superconducting transition as seen in Fig.5a) provides strong evidence for vortex-dominated electrical properties of the tin-decorated graphene.

4.2. Comparison of samples

Fig.5d) shows the response to a perpendicular magnetic field for two samples, $Sample1$ and $Sample2$. For weak magnetic fields, the normalized depinning current (I_d) of $Sample2$ decreases more abruptly when the absolute value of the perpendicular magnetic field is increased. This enhanced sensitivity can be attributed to the arrangement of the tin islands. Indeed, the larger the pancake-like tin islands are, the closer they are. The magnetic field expelled by Meissner effect in the tin islands is more confined in the interstitial area in graphene at the core of each Josephson junction. Since more tin was deposited on $Sample2$, the interstitial areas are thinner than for $Sample1$. It results in a strong magnetic field focusing effect in the weak link regions. This strong sensitivity of the depinning current (I_d) to small magnetic fields applied perpendicular to the film is typical for weak links [44]. Nevertheless, out of the weak magnetic field regime, the normalized depinning current (I_d) for $Sample2$ is higher than for $Sample1$. Thus, for higher values of the magnetic field, the greater surface covering of graphene by the tin islands for $Sample2$ compensates the effect of magnetic field confinement. The critical magnetic field (H_c) is more than twice higher for $Sample2$ compared to $Sample1$. Although the surfaces and aspect ratios of the two samples are of the same order, the switching current (I_s) measured at weak perpendicular magnetic field ($H_\perp = 1.1mT$) for $Sample2$ was also about more than twice larger than the one of $Sample1$ as can be seen in Fig.5c). These observations are consistent with the fact that the Josephson junctions are shorter in $Sample2$ for which more tin has been evaporated than in $Sample1$.

The emergence of a large plateau in the superconducting transition of the $Sample2$ shown in Fig.5c) corresponds to a regime where the vortices reach a constant speed of motion giving rise to a constant value for the probed differential resistance. This plateau is absent for the same value of perpendicular magnetic field for the superconducting transition of the $Sample1$ in Fig.5c) because the smaller value of the switching current I_s induces a sharp transition towards the resistive normal state before the vortices reach their constant motion speed regime.

The transition from the resistive normal state to the superconducting state has not exactly the same shape as the transition from the superconducting state to the resistive normal state as one can see on Fig.5b). This hysteretic behaviour is stronger

for *Sample*2 because of the larger thickness of both the superconducting tin islands and the parylene substrate that prevent the heat from being efficiently evacuated.

5. Conclusions

In conclusion, we build a mechanically-flexible graphene-based metal coated thin film exhibiting tunable superconducting properties at low temperature. The non-covalent coupling of the graphene with the two other top and bottom components allows the graphene to keep its exceptional electronic properties, while gaining novel properties such as tunable superconductivity even when graphene supports only a few-nanometer-thick discontinuous metallic film. The sensitivity to the external environment is enhanced thanks to the hybrid 2D behavior of the film. Especially, the superconducting correlations in the graphene interface are highly sensitive to a perpendicular magnetic field and is tunable with an electric field thanks to the preserved semi-metallic properties and the 2D character of the graphene. This work highlights the potential of graphene as a versatile building-block for the realization of macroscopic plastic-like superconductors with high supercurrent density comparable to single Josephson junctions. The very low volumic mass of parylene C (1.289 g.cm^{-3}) allows to get superconducting films with very low area density (about 5g.m^{-2}) compared to pure tin superconducting thin film whose weight is around six times higher. Flexible superconducting thin composite films could provide a physically-compact, easily processable by plasma etching into multiwire flexible flat cables. Flexibility and superconductivity respectively provide vibrational and thermal insulation useful for multistage cryostat [45] in which pulse-tube technology require vibrational damping. On a more fundamental side, this material offers a novel playground to study collective proximity effect at the macroscopic scale.

Acknowledgments

J.R. acknowledges support from Grenoble Alpes University community (AGIR-2016-SUGRAF). The authors are grateful for the help from NanoFab team of Institut Néel. This work is supported by the following contracts of Agence Nationale de la Recherche: J2D project grant (ANR-15-CE24-0017) GRAPHMET (ANR-16-CE09-0016) and DIRACFORMAG (ANR-14-CE32-0003) , and partially supported by the EU FP7 Graphene Flagship (project no. 604391).

References

[1] Judeinstein P and Sanchez C 1996 *J. Mater. Chem.* **6** 511–525

[2] Oriakhi C O 2000 *Journal of Chemical Education* **77** 1138

[3] Carraro M and Gross S 2014 *Materials* **7** 3956–3989

[4] Feigel'man M V, Skvortsov M A and Tikhonov K S 2008 *JETP Letters* **88** 747–751

[5] Kessler B M, Girit c O, Zettl a and Bouchiat V 2010 *Physical Review Letters* **104** 1–4

[6] Allain A, Han Z and Bouchiat V 2012 *Nature Materials* **11** 1–5

[7] Von Metzen R P and Stieglitz T 2013 *Biomedical Microdevices* **15** 727–735

[8] Hopcroft M a, Nix W D and Kenny T W 2010 *Journal of Microelectromechanical Systems* **19** 229–238

[9] Lee C, Wei X, Kysar J W and Hone J 2008 *Science* **321** 385–388

[10] Tsai H l, Schindler J L, Kannewurf C R and Kanatzidis M G 1997 *Chemistry of Materials* **9** 875–878

[11] Kryszewski M 2000 *Synthetic Metals* **109** 47–54

[12] Caironi M, Anthopoulos T D, Noh Y Y and Zaumseil J 2013 *Advanced Materials* **25** 4208–4209

[13] Mitzi D B, Chondroudis K and Kagan C R 2001 *IBM J. Res. & Dev.* **45** 29–45

[14] Li X, Cai W, An J, Kim S, Nah J, Yang D, Piner R, Velamakanni a, Jung I, Tutuc E, Banerjee S K, Colombo L and Ruoff R S 2009 *Science* **324** 1312–1314

[15] Kim M, Shah A, Li C, Mustonen P, Susoma J, Manoocheri F, Riikonen J and Lipsanen H 2017 *2D Materials* **4** 035004

[16] Lee J E, Ahn G, Shim J, Lee Y S and Ryu S 2012 *Nature Communications* **3** 1024

[17] Jakabovič J, Kováč J, Weis M, Haško D, Srnánek R, Valent P and Resel R 2009 *Microelectronics Journal* **40** 595–597 ISSN 00262692

[18] Park D W, Brodnick S K, Ness J P, Atry F, Krugner-Higby L, Sandberg A, Mikael S, Richner T J, Novello J, Kim H, Baek D H, Bong J, Frye S T, Thongpang S, Swanson K I, Lake W, Pashaie R, Williams J C and Ma Z 2016 *Nature Protocols* **11** 2201–2222

[19] Huang M, Yan H, Chen C, Song D, Heinz T F and Hone J 2009 *Proceedings of the National Academy of Sciences* **106** 7304–7308

[20] Huang M, Yan H, Heinz T F and Hone J 2010 *Nano Letters* **10** 4074–4079

[21] Mohiuddin T M G, Lombardo a, Nair R R, Bonetti a, Savini G, Jalil R, Bonini N, Basko D M, Galiotis C, Marzari N, Novoselov K S, Geim a K and Ferrari a C 2009 *Physical Review B - Condensed Matter and Materials Physics* **79**

[22] Bendiab N, Renard J, Schwarz C, Reserbat-Plantey A, Djevahirdjian L, Bouchiat V, Coraux J and Marty L 2018 *Journal of Raman Spectroscopy* **49** 130–145

[23] Yan J, Zhang Y, Kim P and Pinczuk A 2007 *Physical Review Letters* **98** 1–4

[24] Das a, Pisana S, Chakraborty B, Piscanec S, Saha S K, Waghmare U V, Novoselov K S, Krishnamurthy H R, Geim a K, Ferrari a C and Sood a K 2008 *Nature Nanotechnology* **3** 210–215

[25] Yoon D, Son Y W and Cheong H 2011 *Physical Review Letters* **106** 155502

[26] Skoblin G, Sun J and Yurgens A 2017 *Applied Physics Letters* **110** 3–7

[27] Das a, Chakraborty B, Piscanec S, Pisana S, Sood a K and Ferrari a C 2009 *Physical Review B - Condensed Matter and Materials Physics* **79** 1–7 ISSN 10980121 (*Preprint* `0807.1631`)

[28] Matthias B, Geballe T and Compton V 1963 *Reviews of Modern Physics* **35** 1–22

[29] Eisenstein J 1954 *Reviews of Modern Physics* **26** 277–291

[30] Heersche H B, Jarillo-Herrero P, Oostinga J B, Vandersypen L M K and Morpurgo A F 2007 *Nature* **446** 56–59

[31] Komatsu K, Li C, Autier-Laurent S, Bouchiat H and Guéron S 2012 *Physical Review B* **86** 115412

[32] Zant H V D, Elion W J W, Geerligs L J, Mooij J E, van der Zant H S J, Elion W J W, Geerligs L J and Mooij J E 1996 *Physical Review B* **54** 10081–10093

[33] Fulton T a and Dunkleberger L N 1974 *Journal of Applied Physics* **45** 2283–2285

[34] Skocpol W J, Beasley M R and Tinkham M 1974 *Journal of Applied Physics* **45** 4054–4066
[35] Courtois H, Meschke M, Peltonen J T and Pekola J P 2008 *Physical Review Letters* **101** 1–4
[36] Parylene properties and characteristics http://www.vp-scientific.com/parylene_properties.htm accessed: 2018-03-30
[37] Shaw R W, Mapother D E and Hopkins D C 1960 *Physical Review* **120** 88–91
[38] Hsu Y J, Lu S Y and Lin Y F 2006 *Small* **2** 268–273
[39] Calado V E, Goswami S, Nanda G, Diez M, Akhmerov a R, Watanabe K, Taniguchi T, Klapwijk T M and Vandersypen L M 2015 *Nature Nanotechnology* **10** 761–764
[40] Durkin M, Mondragon-Shem I, Eley S, Hughes T L and Mason N 2016 *Physical Review B* **94** 1–8
[41] Xia W and Leath P L 1989 *Physical Review Letters* **63** 1428–1431
[42] Leath P L and Xia W 1991 *Physical Review B* **44** 9619–9633
[43] Gor'kov L and Kopnin N 1975 *Uspekhi Fizicheskih Nauk* **116** 413
[44] Mannhart J, Chaudhari P, Dimos D, Tsuei C C and McGuire T R 1988 *Phys. Rev. Lett.* **61**(21) 2476–2479
[45] Tuckerman D B, Hamilton M C, Reilly D J, Bai R, Hernandez G A, Hornibrook J M, Sellers J A and Ellis C D 2016 *Superconductor Science and Technology* **29** 084007

Supplementary materials of article : "Highly flexible superconducting films with metal-decorated composite 2D materials" by P. Ronseaux et al.

1. Details of the fabrication methods

1.1. CVD graphene

Graphene was grown using the classical method based on CVD on copper [1, 2] using a 18 μm-thick copper foil, which enables batch fabrication of high-quality large-area graphene monolayers at several centimeters scale. The first step of the process consists in ramping up the temperature of the furnace until 1000°C while flowing 100 sccm of Ar and 10 sccm of H_2. Then, an annealing at 1000°C during one hour with 50 sccm of H_2 and 100 sccm of Ar is done. A flow composed of 5 sccm of CH_4, 70 sscm of H_2 and 630 sccm of Ar during 1800 seconds is required for the following growth step. To finish, the temperature is progressively decreased with a flow of 630 sccm of Ar.

1.2. Graphene on micrometer thick parylene C substrates

We used a direct physical vapor deposition (PVD) of parylene C on the CVD grown graphene/Cu film [3]. Recent works had shown that this technique allows to get graphene/parylene structures with a sheet resistance extremely resilient to strain : it can withstand 6% of strain and bending down to a radius of 0.25 mm without much change in conductivity [3]. The process used for the vapor deposition follows the recipe described by Kim *et al.* [3]. During the deposition, parylene is initially vaporized from its solid dimer phase inside a vaporizer furnace at 140°C. Next, the dimers flows to a high-temperature furnace at 690°C, where methylene-methylene bonds are broken, converting the dimers to monomers. In the last stage, the polymerization of the monomer takes place at room temperature on the substrate surface inside a deposition chamber at a pressure of around 100 mbar. Then, the Cu substrate is etched in a solution made of $(NH_4)_2S_2O_8$ (1g of $(NH_4)_2S_2O_8$ powder for 10mL of water) to achieve a freestanding graphene/parylene C film. To finish, the graphene/parylene C is cleaned under water flow.

1.3. Tin deposition

The hybrid Sn/graphene device is obtained by self assembly of an array of Sn clusters during metal evaporation thanks to the Sn diffusion on the exposed surface of graphene. The tin is evaporated under vacuum (pressure $\approx 10^{-6}$ mbar), at room

temperature. Due to the low melting point of tin (232°C) and its poor wettability on the surface of graphene [4], the metal spontaneously self-organizes into non-percolating several nm-thick pancake-like islands. In the gap between the tin islands, there is no metal on top of graphene. The mean gap size is about 20nm, which corresponds to roughly 10% of the islands size. The island density is about 100 per micron square, which leads to a rapid averaging of mesoscopic fluctuations in macroscopic devices such as the ones we study in this work. At the end of this process we obtain a few micrometers thick macroscopic composite film based on two types of nanomaterials in strong interaction, a set of tin nanocluster physisorbed on graphene. They are both supported by a plastic film formed by the parylene polymer. The network of tin islands is connected through the semi-metallic graphene interface forming a 2D array of Josephson junctions. The composite film sketched in Fig. 1 of the main text is named $Sample1$ ($Sample1$: 15 nm Sn/graphene/4 μm parylene C). Another sample has been fabricated following the same process ($Sample2$: 20 nm Sn/graphene/10 μm parylene C). Most of the results presented in this article are from the measurements done on $Sample1$.

2. $R_n \cdot I_s$ product for $Sample1$

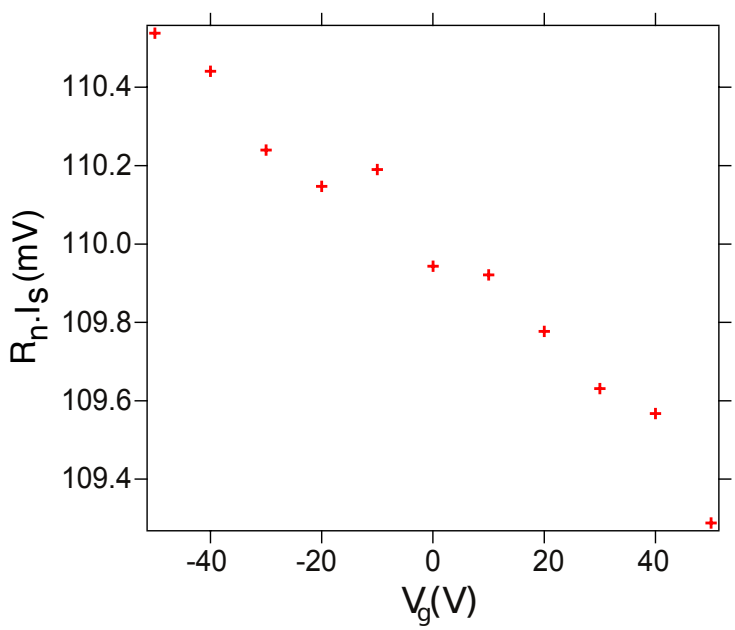

Figure S1. $R_n \cdot I_s$ **product for** $Sample1$**.**

The relevant quantity that should be considered when assessing the coupling strength of a SNS single junction is the product between the normal state resistance (R_n) and the critical current (I_c). Let us emphasise that the critical current (I_c) might differ from the experimentally determined switching current (I_s) [5]. For a single tunnel junction with superconducting tin characterized by an energy gap Δ_0 of 1.15meV [6], the

$R_n \cdot I_c$ product at 0K given by the Ambegaokar-Baratoff formula [7, 8]($R_n \cdot I_c = \pi \frac{\Delta_0}{2e}$) is 1.81mV. For metallic links, the $R_n \cdot I_s$ product can be up to twice larger [9]. The $R_n \cdot I_s$ product of $Sample1$ is displayed in Fig.S1 considering that the experimentally probed switching current I_s is close to the theoretical critical current I_c (which is a reasonable assumption regarding the presence of highly filtered lines in the cryostat). This $R_n \cdot I_s$ product is about 110mV at V_g=0V. It is almost two orders of magnitude larger than for a single tin based Josephson junction. This high value of the probed $R_n \cdot I_s$ product comes from the fact that we probed a Josephson junctions array.

Let us define the length L and width W. The length L is linked to the number M of single Josephson junctions in series in the direction of the current flow. The width W is determined by the number N of Josephson junctions in parallel. As R_n is proportional to $\frac{M}{N}$ [10] and I_s increases with N, the $R_n \cdot I_s$ product would be proportional to M. Nevertheless this model can not explain satisfactorily the measured $R_n \cdot I_s$ product for $Sample1$ since it is about 10^3 smaller than the number of series single junctions along the line between the probes.

In the macroscopic disordered composite, the Josephson junctions chains are not completely independent. Hence, the supercurrent can percolate, opening paths of current flow through chains that are not necessarily straight and parallel to the length L. Moreover, all the single junctions of the array are not homogeneous. Global superconducting area gathering the strongest links can form around a weaker link, giving rise to effective junctions. The probed switching current I_s may be determined by the weakest link along the strongest chain of the array. Thus, the probed $R_n \cdot I_s$ product would be different than the one expected for the perfect array model.

3. Variation of the switching current (Is) with temperature for $Sample1$

The Ambegaokar-Baratoff equation for the temperature dependence of the critical current of a single Josephson Junction [11] fits reasonably well the experimental data (see Fig.S2). This shows that the critical behaviour of the macroscopic composite film corresponds to the one of single Josephson junction. The critical temperature T_c estimated from the fit is 2.66 K which is reduced compared to the one for bulk tin. This value is more reliable than the one deduced from the differential resistance ($\frac{dV}{dI}$) variation with temperature (see Fig.3a) and the corresponding section 3.2 in the main text).

4. Detailed behaviour for $Sample2$

The Fig.S3 is the complete dataset from which have been extracted the curves showing the enhanced sensitivity to a perpendicular magnetic field and the high switching current density for $Sample2$ (see Fig.5 c) and d) and the corresponding section 4 in the main text). The bias current (I_b) span was not large enough to reach the switching current (I_s) at zero perpendicular magnetic field. Normalizing with the

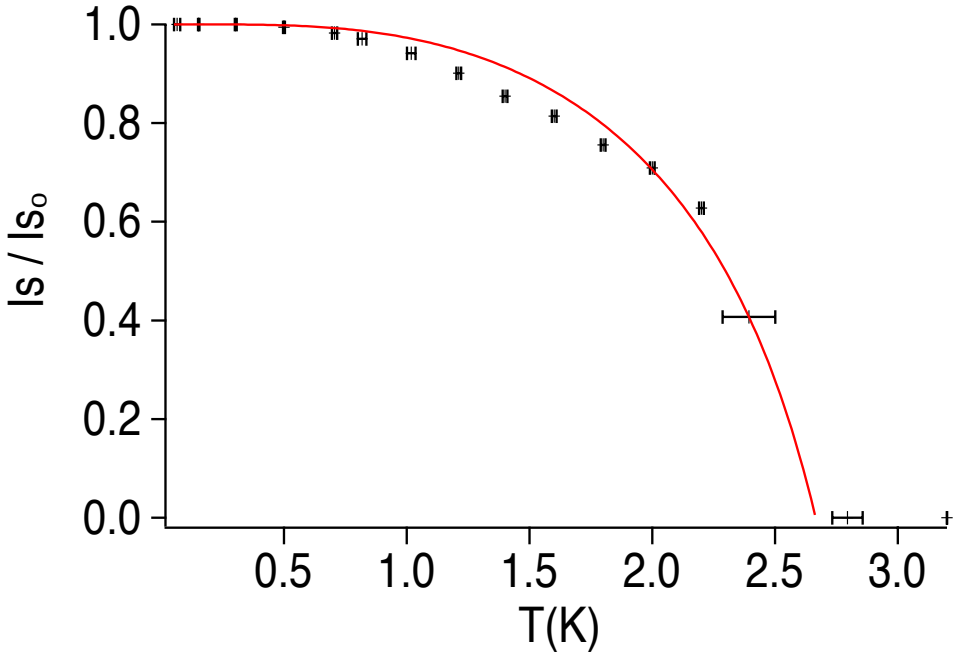

Figure S2. Evolution of the normalised switching current (I_s) with temperature for *Sample*1. The black points are the experimental data with error bars. The solid red line refers to the theory of Ambegaokar-Baratoff.

diameter of our probes of 1mm when no perpendicular magnetic field is applied, we get a density of supercurrent (J_s) higher than 3.10^2 nA $\cdot\mu$m^{-1}. This high value, which is about twice the density of supercurrent (J_s) for *Sample*1, emphasizes the fact that the critical behaviour of the macroscopic composite film corresponds to the one of a single Josephson junction [12]. The important hysteretic behaviour is due to the 10μm-thick parylene which does not allow efficient evacuation of heat (see Fig.5 b) and the corresponding section 4 in the main text).

5. Estimation of the parylene substrate capacity C_s for *Sample*1

The parylene substrate capacity C_s was estimated from the variation of the SNS array of junctions conductance (G) with the applied back gate (V_g) at 4K for *Sample*1, featured in the inset on Fig.3b) (main text). For the estimation of the parylene substrate capacity C_s, the relative permittivity was set to 3, which is the value of its real part at 100K and a few tens of Hertz [13]. We used a planar capacitor model : $C_s = \frac{\epsilon_0 \cdot \epsilon_r}{d}$, where d is the parylene C substrate thickness, ϵ_0 is the vacuum permittivity and ϵ_r is the relative permittivity. As the parylene C substrate thickness d is 4μm, $C_s = 6.63 \cdot 10^{-10}$ F.cm^{-2}. We then deduce the electron density (Δn) dependence on back gate voltage (V_g) : $\Delta n = \frac{C_s \cdot V_g}{q}$, where q is the elementary charge, to scale the top and bottom axis of Fig.3b of the main text.

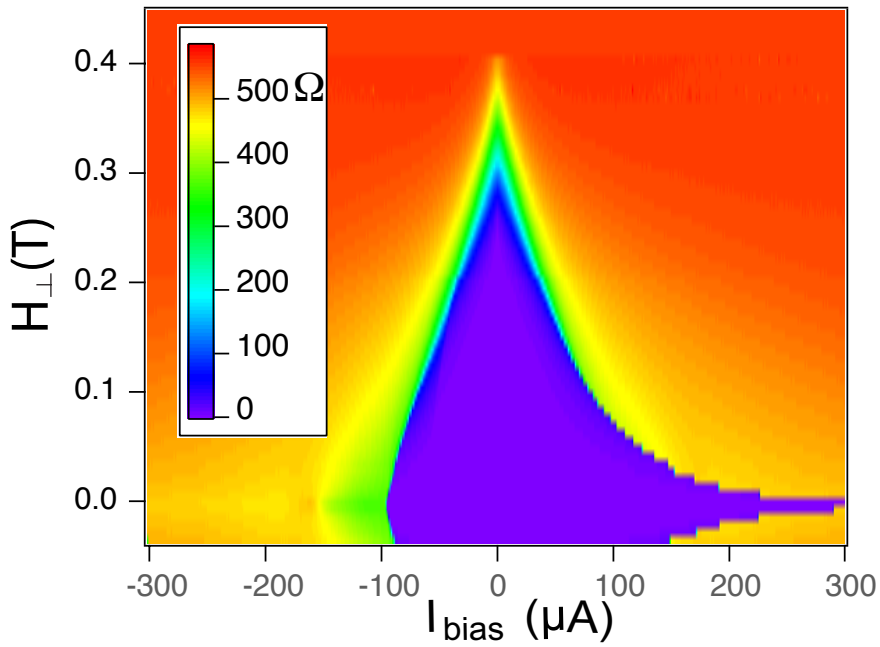

Figure S3. Perpendicular magnetic field dependence for *Sample*2 SNS junctions array differential resistance $\frac{dV}{dI}(Ib)$ as a function of transverse magnetic field ($H_\perp$) and bias current (I_b).

6. Estimation of the mobility for *Sample*1

The general formula used to calculate the mobility is : $\mu = \left(\frac{\Delta\sigma_{sq}}{\Delta n}\right) \cdot \frac{1}{q}$, where $\Delta\sigma_{sq}$ is the variation of the square conductivity (S.□), Δn is the variation of the number of charges (cm^{-2}), q is the elementary charge (C) and μ is the mobility (cm^2.V^{-1}.s^{-1}). As *Sample*1 is square, we considered the conductance G in the inset on Fig.3b) (main text) equal to σ_{sq}. Estimating the ratio $\left(\frac{\Delta\sigma_{sq}}{\Delta n}\right) = 2.64.10^{-16}$ S.cm^2 from the slope in the inset on Fig.3b) (main text), we get $\mu \approx 1640$ cm^2.V^{-1}.s^{-1}.

References

[1] Li X, Cai W, An J, Kim S, Nah J, Yang D, Piner R, Velamakanni a, Jung I, Tutuc E, Banerjee S K, Colombo L and Ruoff R S 2009 *Science* **324** 1312–1314

[2] Han Z, Kimouche A, Allain A, Arjmandi-Tash H, Reserbat-Plantey A, Pairis S, Reita V, Bendiab N, Coraux J and Bouchiat V 2012 *Arxiv preprint arXiv* 4

[3] Kim M, Shah A, Li C, Mustonen P, Susoma J, Manoocheri F, Riikonen J and Lipsanen H 2017 *2D Materials* **4** 035004

[4] Allain A, Han Z and Bouchiat V 2012 *Nature Materials* **11** 1–5

[5] Vion D, Götz M, Joyez P, Esteve D and Devoret M H 1996 *Physical Review Letters* **77** 3435–3438

[6] Townsend P and Sutton J 1962 *Physical Review* **128** 591–595

[7] Tinkham M 1996 *Introduction to superconductivity* (McGraw-Hill)

[8] Ambegaokar V and Baratoff A 1963 *Physical Review Letters* **11** 104

[9] Likharev K 2013 *Journal of Chemical Information and Modeling* **53** 1689–1699

[10] Zant H V D, Elion W J W, Geerligs L J, Mooij J E, van der Zant H S J, Elion W J W, Geerligs L J and Mooij J E 1996 *Physical Review B* **54** 10081–10093

[11] Mannhart J, Chaudhari P, Dimos D, Tsuei C C and McGuire T R 1988 *Phys. Rev. Lett.* **61**(21) 2476–2479

[12] Calado V E, Goswami S, Nanda G, Diez M, Akhmerov a R, Watanabe K, Taniguchi T, Klapwijk T M and Vandersypen L M 2015 *Nature Nanotechnology* **10** 761–764

[13] Kahouli a, Sylvestre a, Ortega L, Jomni F, Yangui B, Maillard M, Berge B, Robert J C and Legrand J 2009 *Applied Physics Letters* **94** 152901